

Carbonaceous matter in the Sariçiçek meteorite

Mehmet YESILTAS ¹, Timothy D. GLOTCH ², Steven JARET², Alexander B. VERCHOVSKY ³,
and Richard C. GREENWOOD³

¹Faculty of Aeronautics and Space Sciences, Kırklareli University, Kırklareli 39100, Turkey

²Department of Geosciences, Stony Brook University, Stony Brook, New York 11794, USA

³School of Physical Sciences, The Open University, Milton Keynes MK7 6AA, UK

*Corresponding author. E-mail: myesiltas@knights.ucf.edu

(Received 25 May 2018; revision accepted 08 March 2019)

Abstract—As of today, the Sariçiçek (SC) meteorite is the newest howardite and the only confirmed fall among the 17 known howardites. In this study, we present isotopic, infrared, and Raman data on three distinct pieces of the SC meteorite. Our oxygen isotopic measurements show that $\Delta^{17}\text{O}$ values of the pieces are close to each other, and are in good agreement with other howardites, eucrites, and diogenites. The carbon isotopic measurements, which were conducted by combusting terrestrial contamination selectively at temperatures lower than 500–600 °C, show the presence of indigenous carbon in the SC specimens. The matrix of these specimens, investigated via infrared microspectroscopy, appears to be dominated by clinopyroxene/orthopyroxene, forsterite, and fayalite, with minor contributions from ilmenite, plagioclase, and enstatite. Carbon-rich regions were mapped and studied via Raman imaging microspectroscopy, which reveals that both amorphous and graphitic carbon exist in these samples. Synchrotron-based infrared microspectroscopy data show the presence of very little aliphatic and aromatic hydrocarbons. The SC meteorite is suggested to be originating from the Antonia impact crater in the Rheasilvia impact basin on 4 Vesta (Unsalan et al. 2019). If this is in fact the case, then the carbon phases present in the SC samples might provide clues regarding the impactor material (e.g., carbonaceous chondrites).

INTRODUCTION

On the late night of September 2, 2015, the Sariçiçek (SC) meteorite fell in the village of Sariçiçek, Bingöl, Turkey. The fall of SC was captured by several cameras in the region, which enabled the recovery of many fragments. Thus far, more than 340 pieces of the meteorite have been recovered from the streets and fields in the Sariçiçek village, totaling to a mass of ~15.24 kg. Based on the petrology, chemistry, and isotopic investigations, SC has been classified as a howardite-type achondrite (Unsalan et al. 2019). Howardites are members of the howardite, eucrite, and diogenite (HED) clan, and are believed to originate from Vestoids, smaller asteroids that were derived by impact processes from 4 Vesta. Based primarily on the evidence from reflectance spectra, asteroid 4 Vesta is

generally considered to be the primary HED source (Consolmagno and Drake 1977; Binzel and Xu 1993).

Carbonaceous matter on 4 Vesta is foreign material, perhaps delivered through impacts by micrometeorites or larger objects. The dark material on Vesta may indicate the presence of impact melts and exogenous carbonaceous material (Reddy et al. 2012). It has been estimated that ~300 low albedo asteroids (diameters 1–10 km) could have impacted Vesta during the last 3.5 Gyr, which would deliver to the Vestan surface ~3–4 × 10¹⁸ g of carbonaceous material (McCord et al. 2012). Howardites are lithified combinations of fragments of eucrites and diogenites (Perron and Zanda 2005), and are heterogeneous breccias with indigenous clasts as well as non-HED materials (Mittlefehldt et al. 1998; Greenwood et al. 2017). Howardites can also contain 2–3% chondritic (CM-like) components (Chou

et al. 1976). Similarly, fragments of CM and CR chondrites were identified in howardites such as Jodzie (Bunch et al. 1979), Kapoeta (Smith 1982), Bholghati (Wang et al. 1990), and Erevan (Nazarov et al. 1995). Jodzie and Bholghati in particular contain up to 5 vol% of carbonaceous chondrite-related material (Zolensky et al. 1996).

Based on its cosmic ray exposure age, radiogenic retention age of ^4He , and the formation age of the Rheasilvia basin, it has been suggested that the SC meteorites may have originated from the 16.75-km diameter Antonia impact crater from the Rheasilvia impact basin on the asteroid 4 Vesta (Unsalan et al. 2019). Here we report the first detailed vibrational spectroscopic data on the SC meteorite samples. We present, in addition to O and C isotopic data, mineralogy and carbonaceous content of the SC fragments with three different sets of infrared data and one set of Raman data. Antonia crater presents both high and low albedo regions, and the darker regions are likely to contain carbonaceous matter that may have been delivered by the impactors. Assuming that the SC meteorite did in fact originate from the Antonia crater, the carbonaceous phases present in the SC fragments may provide important clues concerning the identity of these impactors.

SAMPLES AND EXPERIMENTAL DETAILS

Sample Preparation

We received three fragments, designated as SC15, SC21, and SC183, of the SC meteorite from the SC meteorite consortium. Information on these samples is given in Table 1. From each rock, we first broke off a few small pieces inside an aluminum foil sheet and then used an agate mortar/pestle set to grind them down to a fine powder, from which we collected C isotopic compositions with the aim of determining whether the carbon present in SC is indigenous (see below). Some portion of the powdered sample was also used for the O isotopic measurements. Another batch of grains powdered from different chips of the samples were studied using the synchrotron-based Fourier transform infrared (FT-IR) spectroscopy at the Advanced Light Source (ALS) in Berkeley, California. The remaining fragments were then cut in half to prepare polished thin sections (~50 μm thick). We note that meteorites can be easily contaminated in the laboratory. Phyllosilicate-rich samples can especially be contaminated when brought into close proximity with outgassing contaminant materials such as silicone rubber, grease, or adhesive tapes (Kebukawa et al. 2009). Clear evidence of silicone contamination is a sharp infrared feature at 1261 cm^{-1}

Table 1. Details of the SC stones investigated in this work.

Sample	Mass (g)	Coordinates of find
SC15	7.58	38.9036°N, 40.5949°E
SC21	7.52	38.9024°N, 40.5939°E
SC183	23.98	38.9056°N, 40.6000°E

SC = Sariçiçek.

due to Si-CH_3 in the spectra of meteorites (Kebukawa et al. 2009). In our experiments, all meteorite samples were kept away from any material that contained silicone rubber, grease, or adhesive tape. We show that the contaminant infrared feature at 1261 cm^{-1} is absent in all spectra of the studied samples. Thin section preparation may also contaminate the samples with artificial organic matter (Fries and Steele 2010), which result in stronger aliphatic CH bands near $3000\text{--}2800\text{ cm}^{-1}$ in the infrared spectra. However, the infrared spectra presented here do not have such strong aliphatic CH bands, and therefore organic contamination in our samples is less likely.

In order to be absolutely certain that no carbon contamination had taken place, we cut a fresh thick section from the SC183 rock that was unpolished and unprocessed in any way. Subsequent to cutting, this sample was measured for the purposes of comparison and carbon was observed to be present. Because carbon is also present in this unpolished and unprocessed sample, we believe that carbon contamination has not occurred during the course of this study. Another evidence of indigenous carbon in the studied samples comes from the C isotopic measurements on the powdered and unprocessed fresh grains of the meteorite samples.

Because the meteorite fragments were recovered rather quickly, terrestrial contamination/weathering is also believed to be minimal. We note that we studied only the fresh-cut interior of the samples and did not conduct any experiment on the edges or outer surfaces of the meteorites, where contamination and weathering products are most likely to be found.

C- and O-Isotopic Measurements

Fragments from the interior of each rock were crushed down to a grain size of $5\text{--}30\ \mu\text{m}$. The powdered grains were placed in glass vials and were transported to the facilities at The Open University for carbon and oxygen isotopic measurements.

Carbon isotope analyses have been performed by stepped combustion in the temperature range $200\text{--}1400\text{ }^\circ\text{C}$ with $100\text{ }^\circ\text{C}$ increments, using the Finesse instrument (Verchovsky 2017) in which a carbon-

dedicated triple-collector mass spectrometer works in static mode. The amounts of carbon released (in the form of CO₂) were measured using a calibrated baratron manometer with 1 torr range. The system blank (~1–2 ng C/step, with δ¹³C ~25‰) was used for correcting the raw data. The lowest amount of C measured in any step in our experiments was two to four times the system blank. The precision of the carbon yield δ¹³C measurements are 1% and 0.3‰, respectively. Oxygen isotope analysis was carried out using an infrared laser-assisted fluorination system (Miller et al. 1999; Greenwood et al. 2017). All three of the SC fragments (SC15, SC21, and SC183) were analyzed in duplicate, with each analysis being undertaken on an ~2 mg aliquot of the homogenized powder. Oxygen was released from the samples by heating in the presence of BrF₅. After fluorination, the oxygen gas released was purified by passing it through two cryogenic nitrogen traps and over a bed of heated KBr. Oxygen gas was analyzed using a MAT 253 dual inlet mass spectrometer. Overall system precision, as defined by replicate analyses of our internal obsidian standard (*n* = 38), is: ±0.053‰ for δ¹⁷O; ±0.095‰ for δ¹⁸O; ±0.018‰ for Δ¹⁷O (2σ) (Starkey et al. 2016).

Oxygen isotopic analyses are reported in standard δ notation, where δ¹⁸O has been calculated as: δ¹⁸O = ([¹⁸O/¹⁶O]_{sample}/[¹⁸O/¹⁶O]_{VSMOW} - 1) 1000 (‰) and similarly for δ¹⁷O using the ¹⁷O/¹⁶O ratio. Δ¹⁷O, which represents the deviation from the terrestrial fractionation line, has been calculated using the linearized format of Miller (2002):

$$\Delta^{17}\text{O} = 1000 \ln(1 + \delta^{17}\text{O}/1000) - \lambda 1000 \ln(1 + \delta^{18}\text{O}/1000)$$

where λ = 0.5247, which was determined using 47 terrestrial whole-rock and mineral separates (Miller et al. 1999; Miller 2002).

Mid- to Far-Infrared Attenuated Total Reflectance Spectroscopy

Attenuated total reflectance (ATR) spectra of SC15, SC21, and SC183 were collected on powdered grains in the Vibrational Spectroscopy Laboratory at Stony Brook University using a SmartOrbit ATR apparatus coupled to a Thermo Fisher Nicolet 6700 FT-IR spectrometer with 4 cm⁻¹ spectral sampling and an atmosphere purged of H₂O and CO₂. The spectrometer was equipped with a solid substrate beamsplitter and a thermoelectrically cooled deuterated L-alanine-doped triglycine sulfate (DLATGS) detector with a

polyethylene window for collecting the far-infrared spectra (600–200 cm⁻¹), and with a KBr beamsplitter and a deuterated triglycine sulfate detector with a KBr window for the mid-infrared spectra (4000–400 cm⁻¹). A total of 256 scans were averaged for each far-infrared and mid-infrared spectrum, which were collected separately and later merged together near 500 cm⁻¹. For reference, a background is measured with no sample on the ATR crystal before each measurement. An ATR correction is applied throughout the measurements.

Mid-Infrared Imaging Microspectroscopy

Two-dimensional infrared maps were collected using a Nicolet iN10 MX FT-IR imaging microscope with a conventional thermal light source and a liquid nitrogen cooled mercury cadmium telluride array detector in the Vibrational Spectroscopy Laboratory at Stony Brook University. Infrared spectra were collected in the mid-infrared region (4000–700 cm⁻¹) in reflection mode with 4 cm⁻¹ spectral resolution. For each spectrum, 32 scans were co-added. Hyperspectral image cubes at 25 μm/pixel spatial sampling were acquired from all SC samples.

Infrared chemical distribution maps were generated, and infrared spectra were extracted from various locations of the collected datasets using Omnic software. Due to the large number of the extracted spectra, an in-house LabVIEW program was created that is able to read all infrared spectra at once and output a single data file containing all spectra together. The MATLAB software package was then used to average all FT-IR spectra, and finally the OriginPro software package was used to plot and visualize the average representative infrared spectra.

Synchrotron-Based FT-IR Microspectroscopy

A small portion of each rock was transported, in the form of powder, to the synchrotron facility, ALS, in Berkeley, California for synchrotron-based FT-IR microspectroscopy measurements. The infrared beamline (1.4) at ALS consists of a Nicolet Nic-plan IR microscope with a Schwarzschild objective and a Magna 760 spectrometer coupled to the synchrotron. The infrared data were collected using a HgCdTe detector and a KBr beam splitter between 4000 and 400 cm⁻¹ in transmission mode with 4 cm⁻¹ spectral resolution.

Raman Microspectroscopic Imaging

We conducted our Raman microspectroscopy experiments at the Vibrational Spectroscopy Laboratory

at Stony Brook University using a WiTec alpha300R confocal Raman imaging system equipped with a 532 nm Nd:YAG laser and a 50 \times objective (NA = 0.8). The laser power on the sample surface was always kept below ~ 1 mW to avoid artificial thermal heating of the sample. We collected Raman spectral data on the ground powders of the samples and Raman imaging data on the thin and thick sections. The powders were measured for 30 accumulations for 1 s exposure time. In addition, after locating a region of interest in the field of view of the microscope, two-dimensional Raman intensity maps were collected from predefined areas with ~ 0.5 μm spatial resolution, and a full Raman spectrum was collected at every pixel within the measured area with 0.03 s integration time. With such low power and short exposure time, we believe that there should be no laser-induced damage or heating on the samples. Indeed, the effect of multiple laser shots of a single point in the SC183 sample was checked and we observed no systematic shift in the carbon peak positions (w) and full width half maximas (FWHM) (Γ) after multiple laser shots at 1.5 mW cm^{-2} . The shifts observed ($4\text{--}6$ cm^{-1}) are within the expected range of the carbon peaks (Busemann et al. 2007). The Raman maps for SC21 and SC183 were collected in multiple parts, and were later stitched together using the WiTec Project software package. The stitching resulted in the apparent horizontal stripping in the distribution maps of SC183.

After data collection, we manually removed the artificial cosmic ray lines as well as the background. Chemical distribution maps of individual components were generated by integrating the signal between the endpoints of observed Raman peaks.

Thin section preparation has been reported to potentially modify/disrupt carbonaceous phases, which may lead to modified Raman D and G carbon peak parameters (Pasteris 1989; Fries and Steele 2010). In an effort to eliminate this problem, we collected the Raman imaging data at 2.5 μm depth below the surface in all samples. As a result, the Raman data in this work represent unmodified carbon phases in the samples.

RESULTS

The stepped-combustion method is a powerful technique to discriminate indigenous carbon in meteorites from the terrestrial carbon contamination (Swart et al. 1983; Grady et al. 1997). This technique is used to selectively combust terrestrial contamination at temperatures lower than $500\text{--}600$ $^{\circ}\text{C}$. Similar to Grady et al. (1997), 600 $^{\circ}\text{C}$ is taken in this work as the border between indigenous carbon and terrestrial contamination. In other words, the carbon that is not combusted at

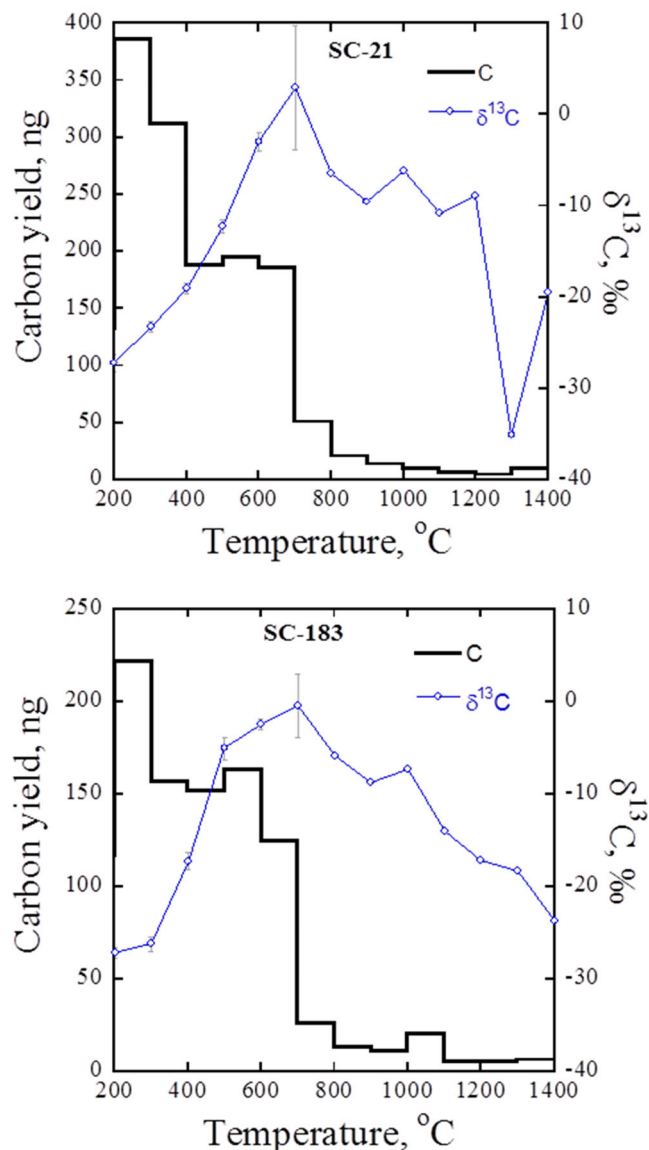


Fig. 1. Graph of carbon yield and $\delta^{13}\text{C}$ against temperature for SC21 and SC183 showing the presence of indigenous carbon in the SC meteorites being combusted above 600 $^{\circ}\text{C}$. (Color figure can be viewed at wileyonlinelibrary.com.)

$T < 600$ $^{\circ}\text{C}$ is extraterrestrial. Figure 1 presents carbon yield in ng and $\delta^{13}\text{C}$ in ‰ against temperature from 200 to 1400 $^{\circ}\text{C}$ in 100 $^{\circ}\text{C}$ steps for SC21 and SC183. Upon combustion, a large amount of carbon is released from SC21 and SC183 at low temperatures until 600 $^{\circ}\text{C}$, which is considered carbon contamination. Therefore, carbon that combusts above 600 $^{\circ}\text{C}$ is likely indigenous to the SC21 and SC183 samples. The isotopic composition of carbon release in this temperature range is significantly heavier than expected for terrestrial contamination. Table 2 presents the values of carbon yields and $\delta^{13}\text{C}$ in the two samples. The $\Delta^{17}\text{O}$ values for

Table 2. Yield and $\delta^{13}\text{C}$ values from SC21 (3.963 mg) and SC183 (4.061 mg) obtained at different temperatures.

Temperature (°C)	SC21		SC183	
	Yield (ng)	$\delta^{13}\text{C}$ (‰)	Yield (ng)	$\delta^{13}\text{C}$ (‰)
200	132.17	-27.2	116.48	-27.1
300	385.47	-23.2	221.39	-26.2
400	312	-19.1	157	-17.3
500	188	-12.3	151.45	-5.1
600	195	-2.9	163	-2.5
700	185	3.0	125	-0.51
800	51	-6.4	26.27	-5.9
900	21	-9.5	13.11	-8.7
1000	14	-6.2	11	-7.3
1100	10	-10.8	20	-14
1200	5.50	-8.9	5.0	-17.2
1300	4.5	-35.1	5.7	-18.2
1400	9.3	-19.5	6.2	-23.7

Table 3. Oxygen isotopic composition of SC meteorite fragments.

Sample	<i>n</i>	$\delta^{17}\text{O}$ ($\pm 1\sigma$)	$\delta^{18}\text{O}$ ($\pm 1\sigma$)	$\Delta^{17}\text{O}$ ($\pm 1\sigma$)
SC15	2	1.770 ± 0.001	3.825 ± 0.024	-0.235 ± 0.013
SC21	2	1.739 ± 0.022	3.780 ± 0.039	-0.242 ± 0.002
SC183	2	1.741 ± 0.012	3.769 ± 0.016	-0.235 ± 0.004

SC = Sariçiçek.

the SC fragments are all close to each other (Table 3), being -0.235‰ , -0.242‰ , and -0.235‰ for SC15, SC21, and SC183 respectively (all $\Delta^{17}\text{O}$ values linearized, see Experimental Details section above for more details). The mean $\Delta^{17}\text{O}$ value for the three SC fragments is -0.237‰ , which is within error of the mean value for eucrite and cumulate eucrite falls and finds of -0.240 ± 0.018 (2σ) obtained by Greenwood et al. (2017). This indicates that the SC meteorite is a normal member of the HED suite and that any carbonaceous chondrite-related component that may be present has had a negligible effect on its oxygen isotope composition.

ATR spectra of the three SC samples display a set of prominent silicate peaks that are mostly due to pyroxene, with some contribution from olivine (Fig. 2). The absorbance peaks near 1009 , 924 , and 883 cm^{-1} are due to Si-O stretching vibrational modes, and are attributed to pyroxene and olivine. The lower frequency region presents the absorbance peaks that are due to Si-O-Si bending vibrational modes. These peaks appear at 726 , 677 , 532 , 479 , 316 , and 233 cm^{-1} and are due to pyroxene (Ca-rich clinopyroxene and Ca-poor orthopyroxene). The peak at 376 cm^{-1} can be attributed

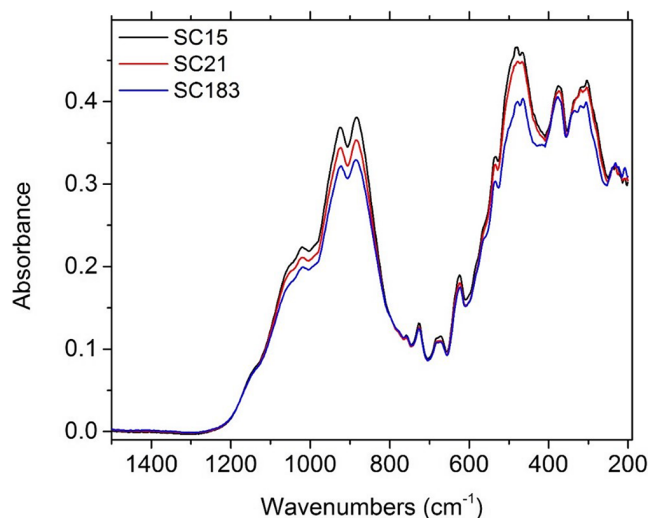


Fig. 2. FT-IR-ATR spectra of the three SC samples collected in the ATR infrared mode. FT-IR = Fourier transform infrared; ATR = attenuated total reflectance. (Color figure can be viewed at wileyonlinelibrary.com.)

Table 4. Positions and assignment of the observed infrared bands.

Wavenumber (cm^{-1})	Wavelength (μm)	Assignment
720	13.88	Pyroxene*
784	12.76	Quartz
815	12.27	Fayalite
833	12.00	Forsterite
869	11.51	Pyroxene
894	11.19	Olivine
916–923	10.92–10.83	Pyroxene*
933	10.72	Fayalite
952	10.50	Forsterite
1024	9.77	Silicates
1039	9.62	Silicates
1060	9.43	Pyroxene*
1118	8.94	Silicates
1135	8.81	Silicates

*Orthopyroxene/clinopyroxene.

to Mg-rich olivine. The infrared bands observed in this study are listed in Table 4.

We measured the SC thin sections using an infrared imaging spectrometer in order to map various mineral phases and their distributions. Figures 3–5 present infrared distribution maps of the most prominent phases observed under the infrared microscope. The numeral in the visible micrograph denotes the spots of phases in the samples, and their corresponding infrared spectra are given on the right panel. The IR spectra were obtained by averaging at least 50 pixels within the

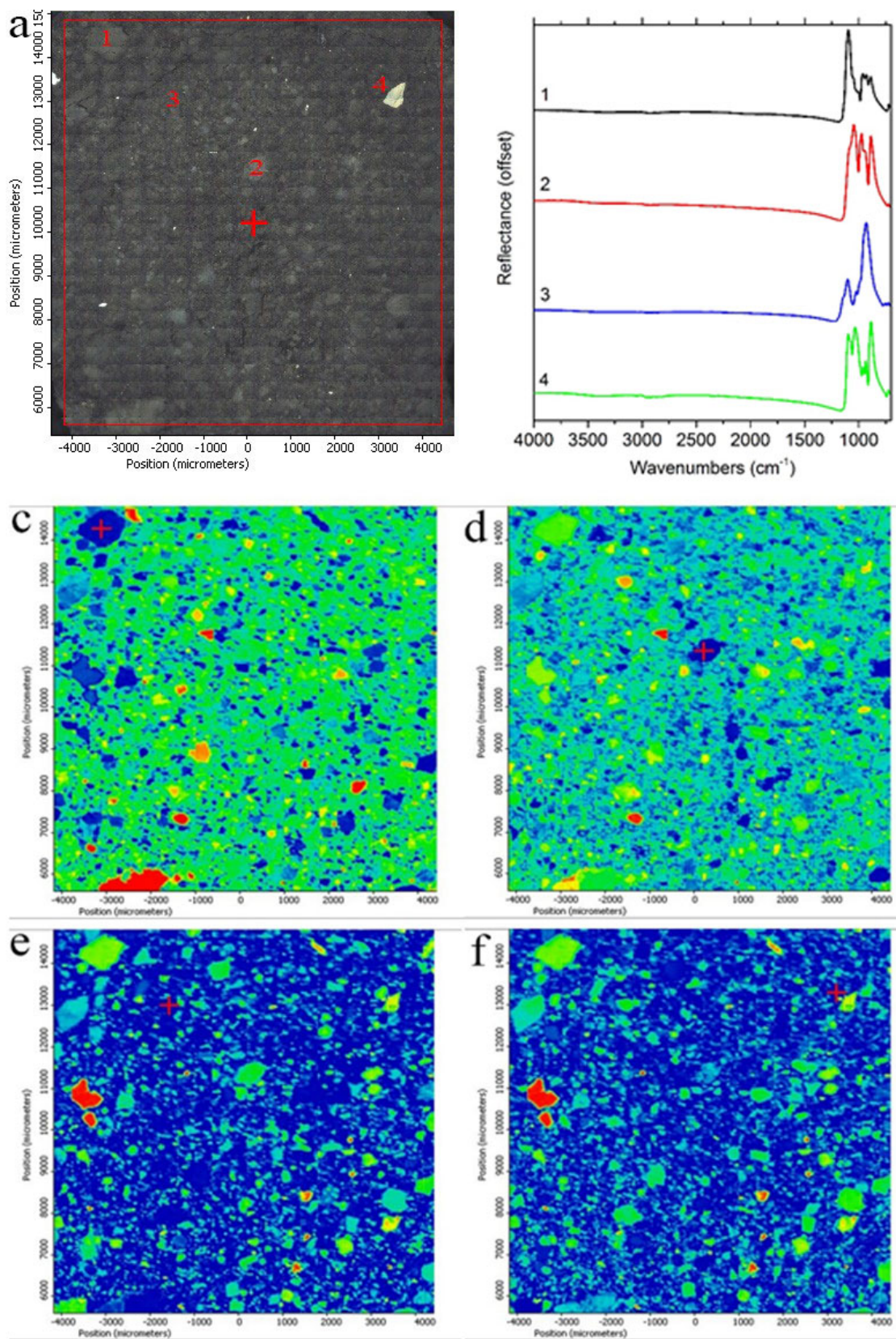


Fig. 3. a) Visible micrograph of SC15. b) Representative infrared reflectance spectra of various grains on the surface of SC15. c–f) Chemical distribution maps generated using the most intense peak height in respective (1–4) infrared spectra (1096, 1045, 935, and 880 cm⁻¹). Rainbow color scale represents reflectance (blue being the highest). (Color figure can be viewed at wileyonlinelibrary.com.)

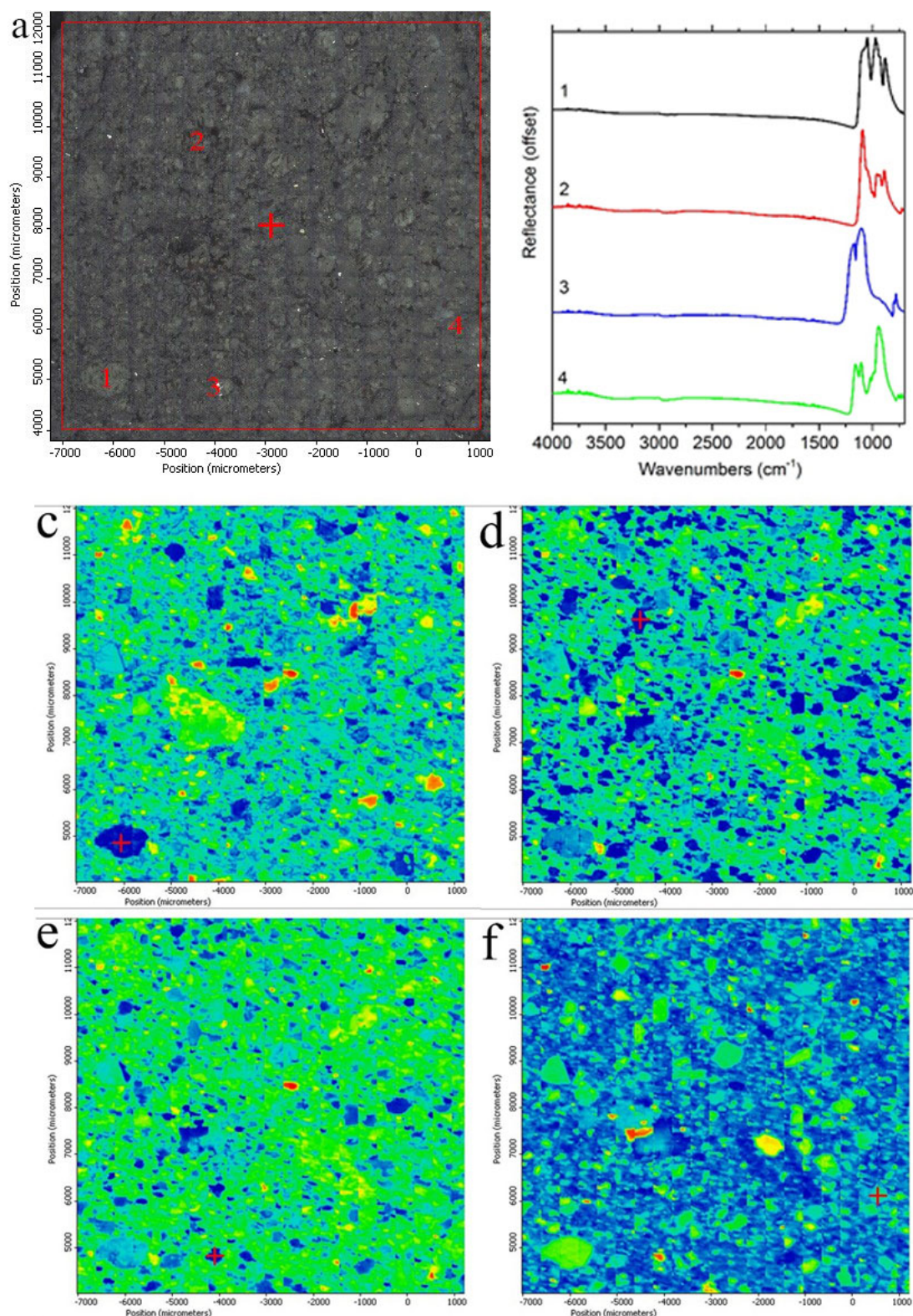


Fig. 4. a) Visible micrograph of SC21. b) Representative infrared reflectance spectra of various grains on the surface of SC21. c–f) Chemical distribution maps generated using the most intense peak height in respective (1–4) infrared spectra (1050, 1094, 1105, and 943 cm^{-1}). Rainbow color scale represents reflectance (blue being the highest). (Color figure can be viewed at wileyonlinelibrary.com.)

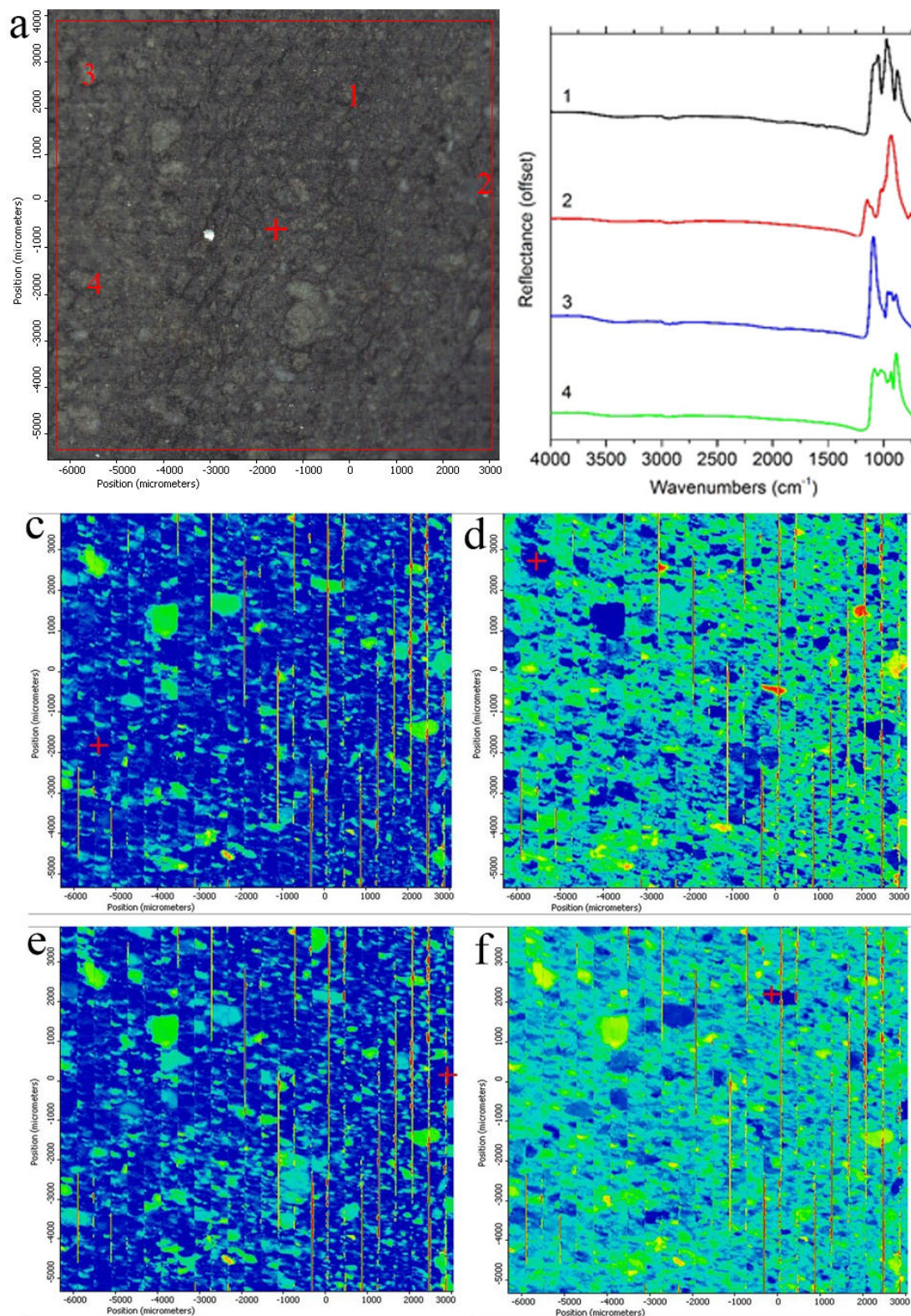


Fig. 5. a) Visible micrograph of SC183. b) Representative infrared reflectance spectra of various grains on the surface of SC183. c–f) Chemical distribution maps generated using the most intense peak height in respective (1–4) infrared spectra (974, 931, 1092, and 886 cm^{-1}). Rainbow color scale represents reflectance (blue being the highest). (Color figure can be viewed at wileyonlinelibrary.com.)

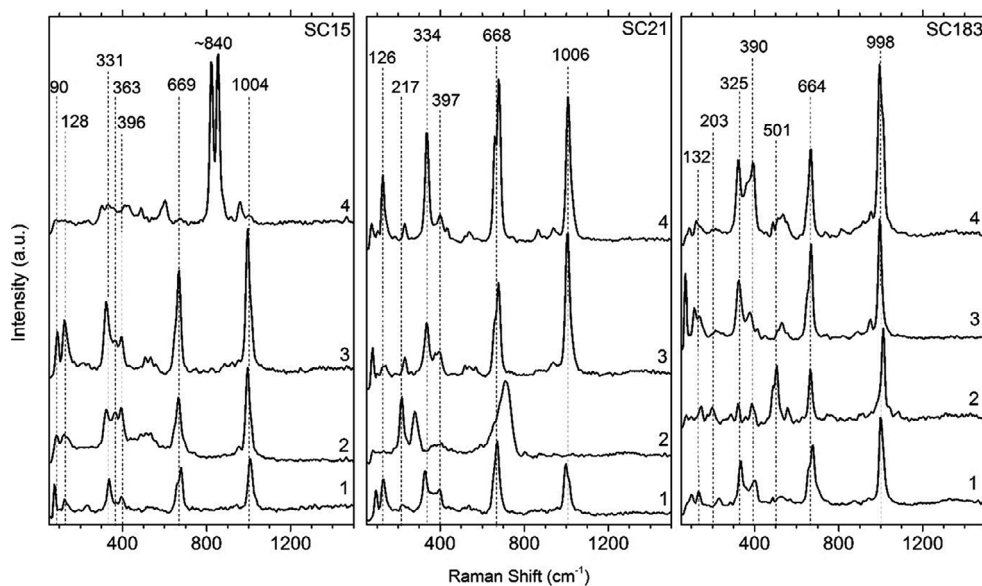


Fig. 6. Raman spectra of powders of SC15, SC21, and SC183. Individual peaks are labeled with their positions. All spectra shown here are attributed to pyroxene minerals, except SC15-4 that is attributed to olivine and SCSC21-2 that seems to be a different type of silicate but unidentified here.

grain of interest, and were offset for clarity. The colors of the infrared maps represent reflectance (blue being the highest). These infrared maps also denote the relative amount of a particular phase, meaning that the more blue the color of a map, the more of that material is present in the measured area. However, we acknowledge that in addition to the mineral abundance, quality of the polish and mineral orientation might also contribute to the infrared peak strength, and therefore to the infrared maps, which cannot be ruled out in this study.

In Figs. 3–5, a doublet centered at 1058 cm^{-1} , due to orthopyroxene and/or clinopyroxene (Hamilton 2000), is observed to be the major phase in the samples. The small feature at 991 cm^{-1} , the doublet at 946 , and the peak at 889 cm^{-1} are due to olivine (mostly fayalite-rich). The individual spectra present other prominent features as well. All three samples present very similar molecular compositions with almost identical inorganic features and infrared bands. The infrared maps help us see spatial distributions of these inorganic phases as well as their frequency of appearance in the meteorite samples. For instance, the infrared distribution map of a material shown in Fig. 3c (SC15) appears to be less compared to the material shown in Fig. 3f, allowing us to relatively infer the abundances. Based on the distribution maps in Figs. 3–5, the matrix of the SC meteorites appears to be dominated by orthopyroxene/clinopyroxene, forsterite, and fayalite, whereas ilmenite, plagioclase, and enstatite seem to appear in smaller amounts.

Raman spectra of the studied samples are consistent with the infrared identifications; however, because our Raman imaging system has a much higher spatial resolution, we are able to identify a wider variety of major and minor phases. Raman spectra of samples SC15, SC21, and SC183 show that the samples are dominated by pyroxene minerals such as augite, diopside, enstatite, kanoite, rhodonite, and ferrosilite. We also observed olivine (Mg-rich) and plagioclase feldspars (anorthite, labradorite) (Fig. 6).

In addition, the Raman spectra at higher frequencies present two prominent carbon peaks, namely D (disordered) and G (graphite) bands located near 1370 and 1600 cm^{-1} , respectively (Busemann et al. 2007). The structural order of the carbonaceous material in each sample was inferred from these Raman bands and their parameters such as positions, intensities, and FWHM. The D band is due to disordered sp^3 carbon bonds, whereas the G band is due to graphite-like sp^2 carbon bonds (Suzuki et al. 2010). In order to investigate these carbon phases, first a linear baseline was subtracted from each hyperspectral data cube between 800 and 1800 cm^{-1} , and cosmic rays were removed wherever present. Using the WiTec Project FOUR+ software, we generated chemical distribution maps for olivine, pyroxene, and carbon for SC15, SC21, and SC183 (shown in Figs. 7–9, respectively) by integrating the signal between a range of frequencies around the respective peak positions.

We then extracted at least 200 Raman spectra from the carbon-rich regions in each meteorite sample. Such

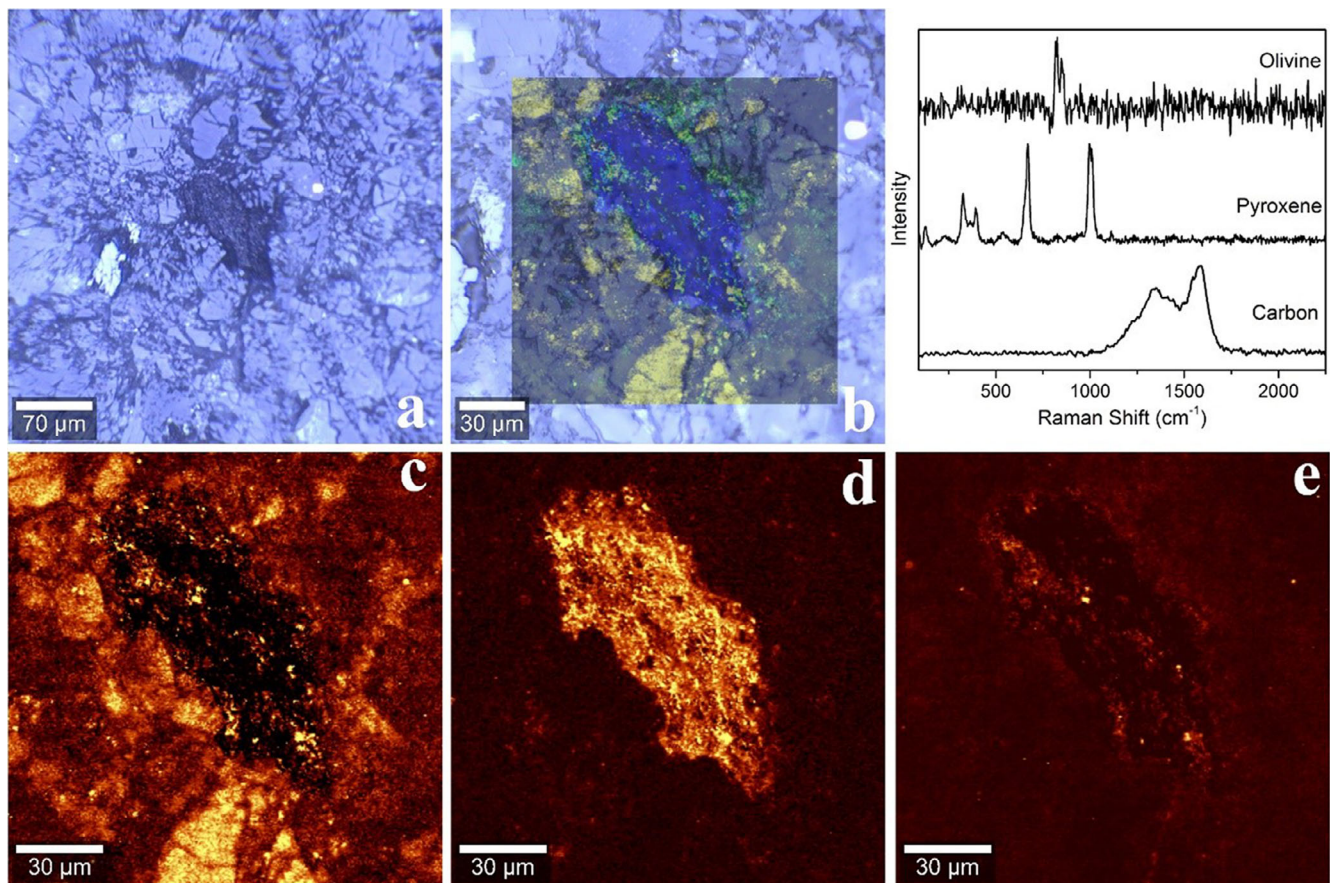


Fig. 7. Raman images and spectra of SC15. a) Visible micrograph of a region of interest containing a dark carbonaceous grain, obtained with a 20 \times objective. b) Visible micrograph of the same region obtained with a 50 \times objective, and pyroxene, olivine, and carbon distribution maps are overlaid. c–e) Intensity distribution maps of pyroxene, carbon, and olivine, respectively. As seen in (e), olivine is only a minor component in the sample, hence the noisy spectrum. The top-right graph presents Raman spectra of the observed chemical components. (Color figure can be viewed at wileyonlinelibrary.com.)

spectra were then fitted with a pair of Lorentzians to determine carbon peak characteristics such as peak centers, widths, and relative intensities of the D and G bands. An example of this fitting is shown in Fig. 10, where the raw spectrum is extracted from the Raman map of SC183. After extracting Raman spectral parameters from at least 200 points, an in-house LabVIEW program was used to read out all the extracted text files for the carbon peak parameters and combine them into a single data file for further analyses.

Figure 11 presents the FWHM of the D and G bands versus their respective center frequencies. The FWHM versus D band does not show any trend; data points from all three samples are distributed near each other. The FWHM versus G band position, on the other hand, shows a linear correlation between the width and the position of the G band. The G-band parameters show a large spread over the frequency of this peak (1552–1600 cm^{-1}) presenting a large spread

over the frequency of this peak, which is likely due to the heterogeneously distributed graphitic domains in the sample. Busemann et al. (2007) also reported that the larger spread of the G band parameters is due to the influence of inhomogeneously distributed relatively large graphitic domains. Therefore, the collected Raman hyperspectral datasets suggest the presence of both amorphous and graphitic carbon domains in the investigated SC fragments.

Thermal processing and histories of parent bodies can be inferred from the Raman spectra (Quirico et al. 2003; Busemann et al. 2007; Bonal et al. 2016). The widths, positions, and intensity ratios of the D and G bands present various trends that can provide clues related to the thermal histories of parent bodies. It was suggested by Wopenka (1988), Quirico et al. (2003), Bonal et al. (2007), and Busemann et al. (2007) that the intensity ratios of the D and G bands (I_D/I_G) provide a trend which is roughly a measure of thermal

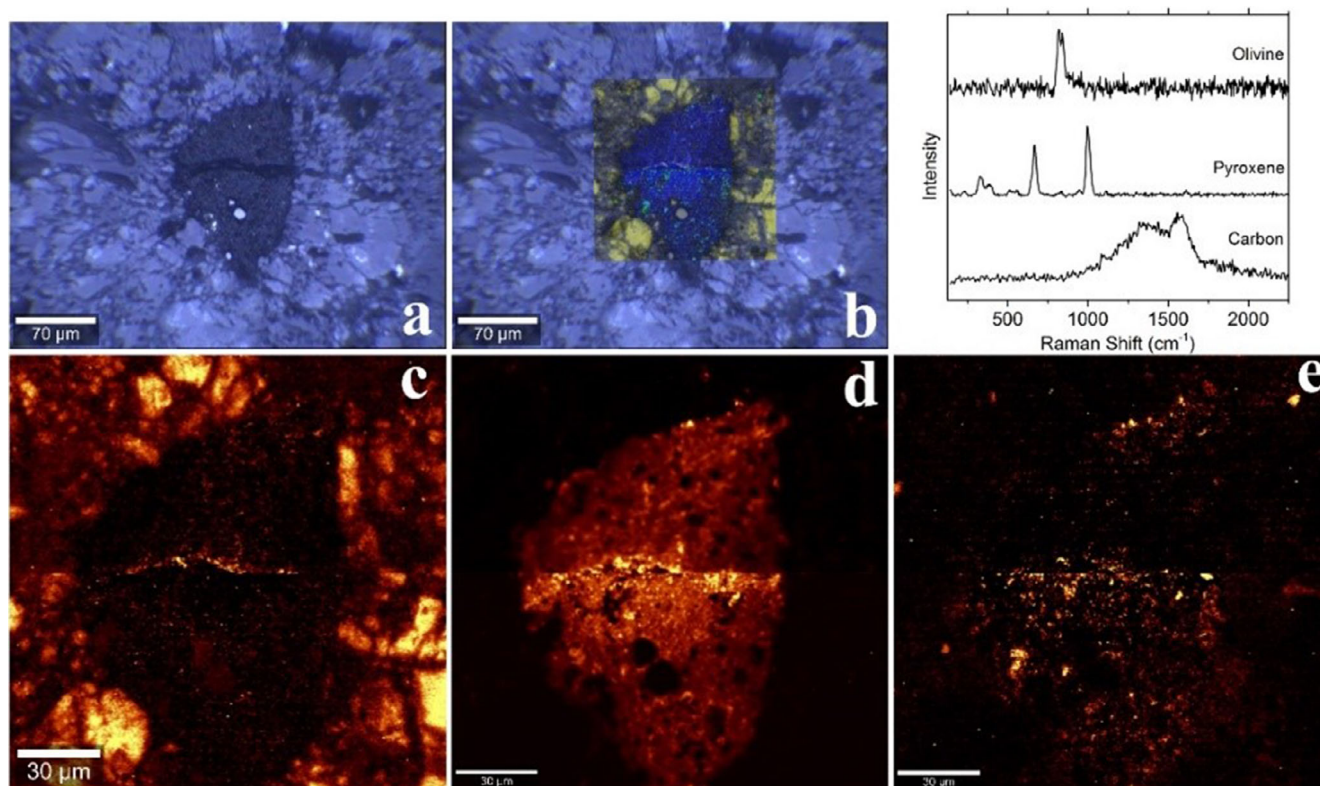


Fig. 8. Raman images and spectra of SC21. a) Visible micrograph of a region of interest containing a dark carbonaceous grain. b) Visible micrograph of the same region where pyroxene, olivine, and carbon distribution maps are overlaid. c–e) Intensity distribution maps of pyroxene, carbon, and olivine, respectively. The top-right graph presents Raman spectra of the observed chemical components. (Color figure can be viewed at wileyonlinelibrary.com.)

metamorphism of the parent body. In order to check the presence of any trends related to thermal metamorphism, we have generated a graph of intensity ratios for all SC samples studied here. Figure 12 presents the width of the D band (Γ_D) versus intensity ratios I_D/I_G for SC15, SC21, and SC183. We see that all three samples and their carbon peak parameters present a linear trend. The three samples, however, are distributed with a small shift in their positions, which may be due to several reasons such as slightly different domain sizes, different structural order, variations in structural defects, and crystal boundary effects (Busemann et al. 2007). Analytical errors might also contribute to the observed variations and they are by no means ruled out. In all cases, SC183 among the three specimens seems to be the intermediate sample based on the carbon peak properties, appearing always between SC15 and SC21 in the graphs.

It has been reported that the D band (and therefore Γ_D) is more sensitive to thermal effects than the G band (Bonal et al. 2016). Here we also present relations of Γ_D and Γ_G with their ratios Γ_D/Γ_G in Fig. 13, where the width of the D band appears to

show a better relation with the width ratios than that of the G band. While the width of the G band spans a relatively narrow range ($\sim 75\text{--}150\text{ cm}^{-1}$), the width of the D band spans a much larger range ($\sim 100\text{--}400\text{ cm}^{-1}$). This behavior indicates that the D band and its spectral parameters reflect thermal metamorphic processes better than those of the G band. In addition, average values (red stars) of the widths of the D and G bands show that structural order of carbon varies slightly for each sample.

DISCUSSION

Based on our stepped combustion experiment, there is some amount of indigenous carbon, released above $600\text{ }^\circ\text{C}$ with $\delta^{13}\text{C}$ variations from 3‰ to -10‰ . These can be represented by graphitic-like forms of carbon. At $1200\text{ }^\circ\text{C}$ and above, the amounts of carbon released are low, and comparable with blank isotopically. The presence of various non-HED components, such as impactor material (e.g., carbonaceous or ordinary chondrites) or terrestrial weathering products, has the potential to cause detectable shifts in the primary

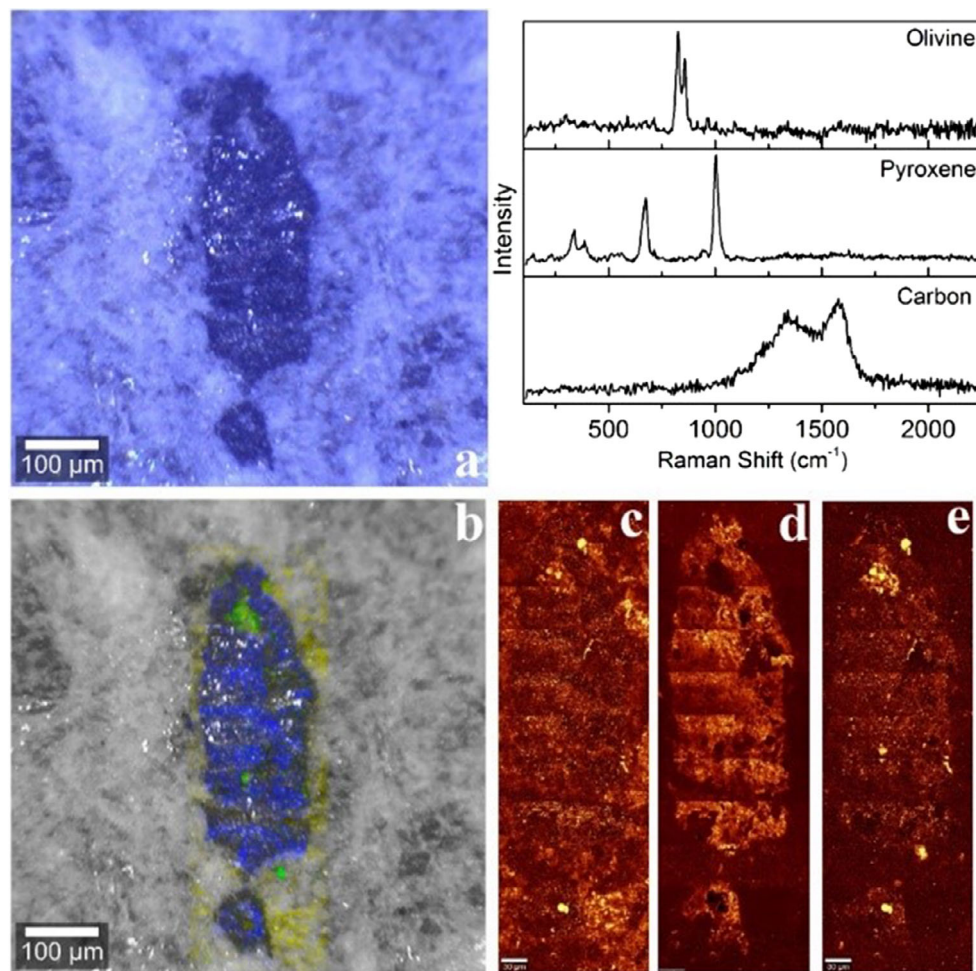


Fig. 9. Raman images and spectra of SC183. a) Visible micrograph of a region of interest containing a dark carbonaceous grain. b) Visible micrograph of the same region where pyroxene, olivine, and carbon distribution maps are overlaid. c–e) Intensity distribution maps of pyroxene, carbon, and olivine, respectively. Top-right graph presents Raman spectra of the observed chemical components. (Color figure can be viewed at wileyonlinelibrary.com.)

oxygen isotopic composition of a meteorite (Greenwood et al. 2017). In particular, howardites containing a significant component of carbonaceous material will be shifted to more negative $\Delta^{17}\text{O}$ values, or in the case of ordinary chondrite-type material the $\Delta^{17}\text{O}$ values will move in the opposite direction (Greenwood et al. 2017). However, in this study, the $\Delta^{17}\text{O}$ values for the SC samples plot within the normal isotopic range of the HED suite and close to the average value of -0.240 ± 0.018 (2σ) (Greenwood et al. 2017). This suggests that the amount of carbonaceous material in the SC meteorites is not significant enough to lower the oxygen isotopic composition outside the gray area shown in Fig. 14.

The more negative $\Delta^{17}\text{O}$ values reported by Unsalan et al. (2019) were interpreted as the result of foreign carbonaceous components in the SC fragments. Addition

of carbonaceous material certainly lowers the $\Delta^{17}\text{O}$ value of HEDs (Greenwood et al. 2017). The samples of SC we have measured do not show any significant lowering of $\Delta^{17}\text{O}$ values compared with the HED average. One possible explanation for the different findings of the two studies is that SC is highly heterogeneous with respect to the amount of carbonaceous chondrite material it contains. The carbonaceous chondrite component in howardites is known to vary considerably from a few percent to as much as 60% in some samples (Herrin et al. 2011). Carbon stepped combustion analysis clearly shows that our samples of SC do contain a carbonaceous chondrite component, but this appears to be insufficient to perturb its primary oxygen isotope composition. We also measured another howardite meteorite, Bholghati, in the same laboratory under the same conditions. Bholghati contains a significant carbonaceous chondrite

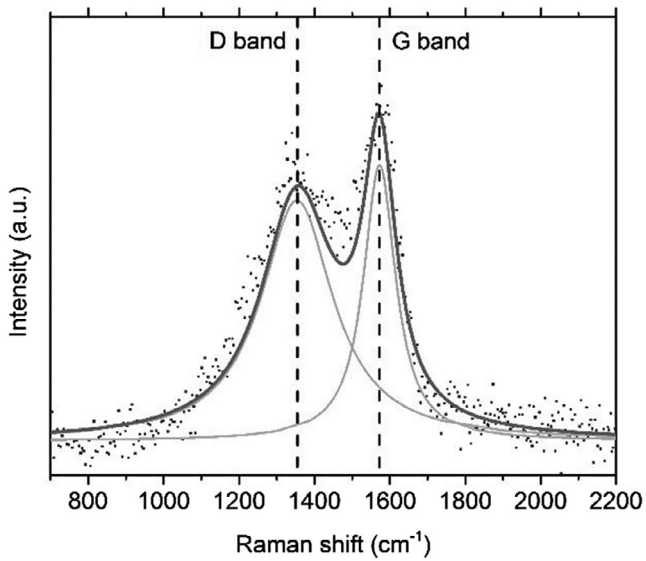


Fig. 10. Lorentzian fitting of a raw spectrum (dotted line) extracted from SC183. The solid lines show the fit peaks (light gray) as well as the cumulative fit peak (dark gray). The vertical dashed lines indicate the positions of the D and G first-order carbon peaks.

component, which lowers the $\Delta^{17}\text{O}$ to fairly negative values. SC has much less carbonaceous component compared with Bholghati. In our case, we found that Bholghati has much lower $\Delta^{17}\text{O}$ values compared with our SC values, which is expected because the latter meteorite contains much less carbonaceous matter. Overall, we remark that in the SC fragments we have analyzed, the carbonaceous component was not present in sufficient amounts to disturb the $\Delta^{17}\text{O}$ value. However, such material would still be detected by the stepped combustion technique.

Busemann et al. (2007) reported thermometric relations based on the Raman peak properties of carbon

present in chondrites. Cody et al. (2008) later proposed a thermometry equation that combines Raman spectroscopy with the thermometric relationships reported by Busemann et al. (2007). While such thermometry estimates roughly indicate the peak thermal metamorphism temperature of the parent body, it is limited to the primitive chondrites (less processed) and it assumes that isothermal heating of a parent body occurred for $\sim 10^7$ years. In the case of Vestoids, particularly in the case of Antonia crater on 4 Vesta, impact heating is a source of short duration heating as opposed to long duration isothermal heating on carbonaceous parent bodies. Even though the carbonaceous material might have been delivered to 4 Vesta through impacts with carbonaceous parent bodies, the collision chemistry and kinetics are quite complicated in the case of achondrites such that the Raman carbon parameters obtained from the carbon phases in the SC fragments may not provide the effective peak thermal metamorphism temperature, thus they are not calculated here.

It cannot be unambiguously concluded that carbonaceous matter penetrated the mineral assemblages only in the final impact, and the processes of crater formation with impacts on the parent body are more complex. However, comparison of Raman spectral characteristics of our data with other meteorites may help constrain the origin of Vesta's dark materials. The average values of each dataset in Fig. 12 (yellow stars) seem to fall near type 3.0–3.05 chondrites reported by Bonal et al. (2016). However, comparison of average Γ_{D} values given as filled red stars in Fig. 13 with that of other meteorites reported by Bonal et al. (2016) shows that the SC samples fall near a CO3 chondrite (MIL 07687) and some other type 2 chondrites reported by Quirico et al. (2014). These comparisons are only qualitative and by no means unambiguous.

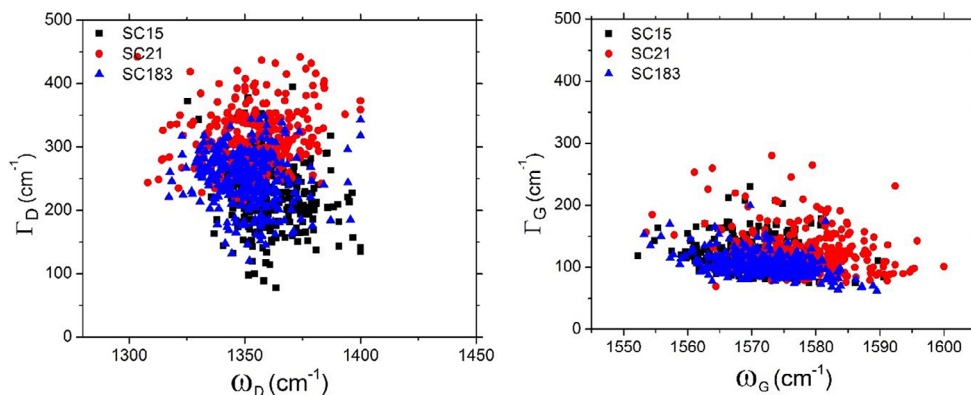


Fig. 11. Raman D and G band parameters of the extracted spectra. FWHM versus ω of D (left) and G (right) carbon bands in SC15, SC21, and SC183. FWHM = full width half maxima. (Color figure can be viewed at wileyonlinelibrary.com.)

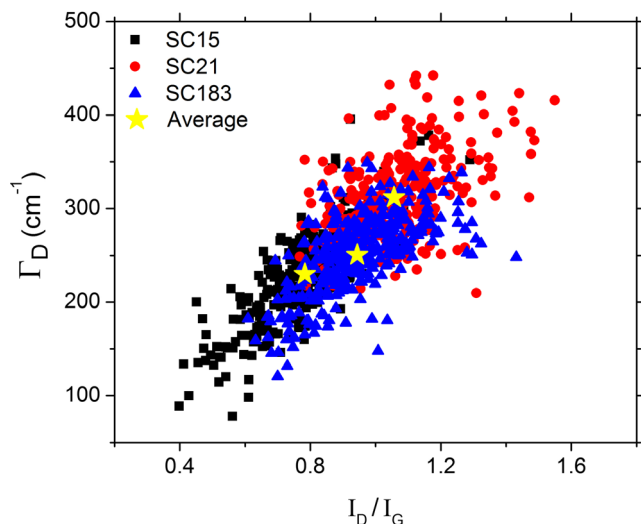


Fig. 12. FWHM of D band versus D and G band intensity ratios. Yellow stars denote the average value of each specimen studied in this work. FWHM = full width half maxima. (Color figure can be viewed at [wileyonlinelibrary.com](#).)

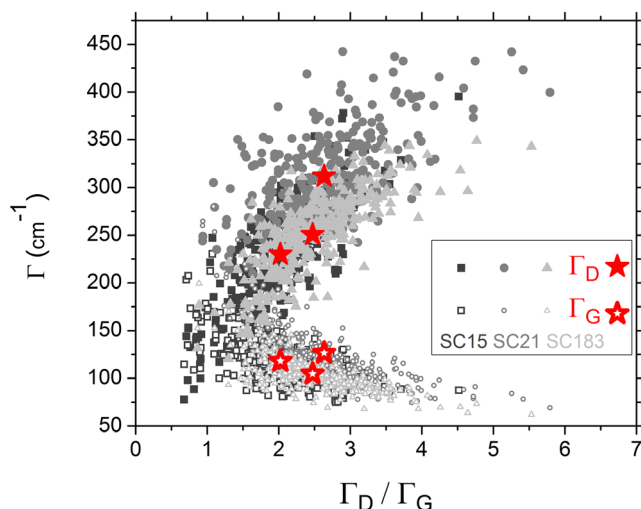


Fig. 13. FWHM of D and G bands versus their FWHM ratios. Filled and empty symbols are for widths of D and G bands, respectively. Squares, circles, and triangles represent SC15, SC21, and SC183, respectively. Red stars denote the average value of each specimen. FWHM = full width half maxima. (Color figure can be viewed at [wileyonlinelibrary.com](#).)

The fact that spectral signatures of carbon are present in our Raman data but not in our infrared data may be due to multiple reasons. One of the reasons is the level of sensitivity of analytical techniques. Infrared spectroscopy is insensitive to highly ordered carbon (graphitic C) and low-hydrogen amorphous carbon (e.g., lack of infrared bands for highly crystalline graphite). On the contrary, infrared spectroscopy is

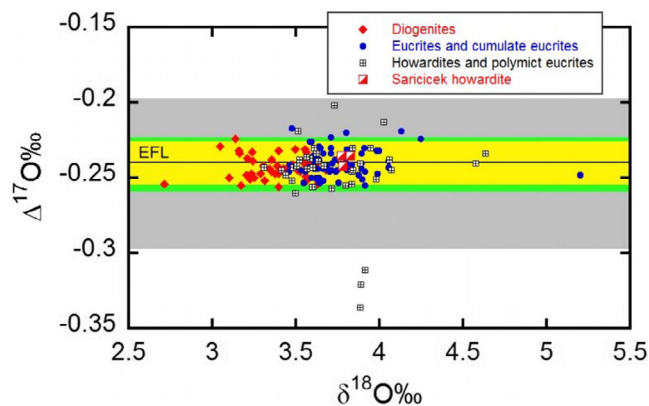


Fig. 14. Oxygen isotopic composition of SC15, SC21, and SC183 compared with other HED meteorites (Greenwood et al. 2017). Yellow area denotes $\pm 2\sigma$ precision for eucrite and diogenite falls. The area between the green lines denotes $\pm 2\sigma$ precision for eucrite, cumulate eucrite and diogenite falls and finds. Gray area denotes $\pm 2\sigma$ precision for howardites and polymict eucrites. EFL = eucrite fractionation line. (Color figure can be viewed at [wileyonlinelibrary.com](#).)

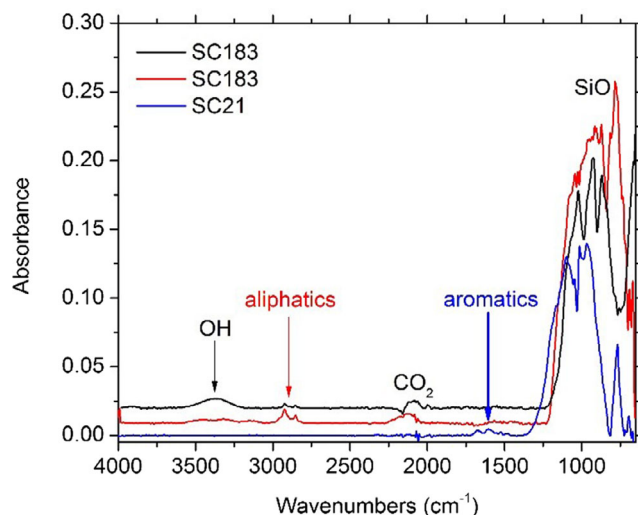


Fig. 15. Synchrotron-based FT-IR spectra of SC183 and SC21 grains. Weak but detectable signatures of aromatics and aliphatics are present. FT-IR = Fourier transform infrared. (Color figure can be viewed at [wileyonlinelibrary.com](#).)

sensitive to aliphatic organic matter but Raman spectroscopy is relatively less sensitive (although detectable). Therefore, this case of the two techniques being complementary to each other may be the reason. Another reason could be the superior spatial resolution of our Raman imaging system ($\sim 0.5 \mu\text{m}$) compared with our micro-FT-IR imaging system ($25\text{--}50 \mu\text{m}$), and the sensitivity to carbon phases in the case of infrared is much less in reflection mode than in absorbance, which makes the detection difficult. In addition, carbon

present in the studied samples may be inorganic such as carbon in carbonates; however, we did not observe prominent carbonate peaks in the spectra of SC fragments. Carbon may also be in aliphatic organic matter but our infrared spectral data lack these aliphatic CH peaks near $3000\text{--}2800\text{ cm}^{-1}$ in most of our infrared spectral measurements. In order to check this further, we measured a small portion of the powdered SC fragments using synchrotron radiation as a light source coupled to an FT-IR microscope at the beamline 1.4 of ALS in Berkeley, California, which has a spot size of $10\text{ }\mu\text{m}$. Some of the spectra collected from powder grains present aliphatic CH peaks (Fig. 15), indicating that the resolution is in fact a factor in detecting the organic matter with our micro-FT-IR imaging setup. The carbon may also be in aromatic structures, such as polyaromatic organic matter whose spectral features appear as small and weak lines near $1700\text{--}1500\text{ cm}^{-1}$. Our synchrotron-based infrared spectra also show a set of small features within this region that can be attributed to aromatics (Fig. 13, blue curve). Therefore, we believe that the carbon in the SC fragments studied in this work is likely due in part to aliphatic and aromatic functional groups.

Asteroid 4 Vesta is a relatively bright asteroid with small patches of darker regions (Jaumann et al. 2012; Reddy et al. 2012), which is believed to be from the infall of carbonaceous material (McCord et al. 2012). The SC meteorite is suspected to originate from the 16.75-km diameter Antonia impact crater from the Rheasilvia impact basin on Vesta (Unsalan et al. 2019), which contains bright as well as dark portions. Our C isotopic data indicate the presence of indigenous carbon in the SC samples that may represent poorly ordered graphitic-like forms. If the SC meteorite is in fact from the Antonia impact crater, the carbon phases present in the SC samples might be from a carbon-rich primitive impactor.

CONCLUSIONS

We have presented the first detailed spectral (infrared and Raman) and isotopic (C and O) data on three distinct SC fragments. Our infrared spectral measurements showed that pyroxene minerals, such as orthopyroxene/clinopyroxene, are the most abundant phases present in these samples, with a smaller contribution from olivine (Mg-rich) and quartz. Infrared spatial distribution maps provide information on the spatial distribution of minerals as well as their frequency of appearance in the meteorite samples under the field of view. Based on our infrared maps, the matrix of all SC samples studied in this work is dominated by

orthopyroxene/clinopyroxene, forsterite, and fayalite, while ilmenite, plagioclase, and enstatite seem to appear in smaller amounts. Among the minerals identified via Raman spectroscopy are augite, diopside, enstatite, kanoite, rhodonite, ferrosilite, olivine, and plagioclase feldspars (anorthite, labradorite). Oxygen isotopic measurements demonstrate that SC is a normal member of the HED suite. Carbon isotopic measurements showed that the carbon in the SC samples are partially indigenous and may represent not well-ordered graphitic-like forms. Our Raman spectroscopic investigation identified the presence of carbon by the first-order D and G carbon peaks between 1300 and 1600 cm^{-1} . We observed that there exist variations in the D and G band spectral parameters such as width, position, and intensity, which indicates structural variations in carbon. In addition, Raman spectral profiles indicate the presence of both amorphous and graphitic carbon in the investigated SC fragments. Comparison of peak parameters to the literature data shows that the carbon in the SC fragments falls near type 2–3 chondrites, although this comparison is qualitative and by no means conclusive. On the basis of our results, and assuming that the SC meteorites originate from the Antonia impact crater, we can conclude that Antonia terrain in the Rheasilvia impact basin on 4 Vesta was affected by impacts of primitive impactors.

Acknowledgments—We thank Nezir Ergun, Galip Akengin, and Fahrettin Baydas for the recovery of the studied SC samples. We are indebted to the consortium for providing the meteorite samples. The anonymous reviewers and the editor are thanked for their insightful comments, which significantly improved the manuscript. The staff members of the ALS IR Beamline and C. Legett (Stony Brook University) are also thanked for their assistance during our measurements. This research was supported by the RIS⁴E node (PI: Timothy D. Glotch) of NASA's Solar System Exploration Research Virtual Institute (SSERVI). Oxygen and carbon isotopic analyses at The Open University are funded through a consolidated grant from the UK's Science and Technology Facilities Council (STFC). Jenny Gibson is thanked for her help with oxygen isotope analysis.

Editorial Handling—Dr. Edward Cloutis

REFERENCES

- Binzel R. P., and Xu S. 1993. Chips off of asteroid 4 Vesta: Evidence for the parent body of basaltic achondrite meteorites. *Science* 260:186–191.
- Bonal L., Bourot-Denise M., Quirico E., Montagnac G., and Lewin E. 2007. Organic matter and metamorphic history

- of CO chondrites. *Geochimica et Cosmochimica Acta* 15:1605–1623.
- Bonal L., Quirico E., Flandinet L., and Montagnac G. 2016. Thermal history of type 3 chondrites from the Antarctic meteorite collection determined by Raman spectroscopy of their polyaromatic carbonaceous matter. *Geochimica et Cosmochimica Acta* 189:312–337.
- Bunch T. E., Chang S., Frick U., Neil J., and Moreland G. 1979. Carbonaceous chondrites—I. Characterization and significance of carbonaceous chondrite (CM) xenoliths in the Jodzie howardite. *Geochimica et Cosmochimica Acta* 43:1727–1742.
- Busemann H., Alexander C. M. O. D., and Nittler L. R. 2007. Characterization of insoluble organic matter in primitive meteorites by microRaman spectroscopy. *Meteoritics & Planetary Science* 42:1387–1416.
- Chou C. L., Boynton W. V., Bild R. W., Kimberlin J., and Wasson J. T. 1976. Trace element evidence regarding a chondritic component in howardite meteorites. Proceedings, 7th Lunar and Planetary Science Conference. pp. 3501–3518.
- Cody G. D., Alexander C. O'D., Yabuta H., Kilcoyne A. L., Araki T., Ade H., Dera P., Fogel M., Miltzer B., and Mysen B. O. 2008. Organic thermometry for chondritic parent bodies. *Earth and Planetary Science Letters* 30:446–455.
- Consolmagno G. J. and Drake M. J. 1977. Composition and evolution of the eucrite parent body: Evidence from rare earth elements. *Geochimica et Cosmochimica Acta* 41:1271–1282.
- Fries M. and Steele A. 2010. Raman spectroscopy and confocal Raman imaging in mineralogy and petrography. *Springer Series in Optical Sciences* 158:111–135.
- Grady M. M., Wright I. P., and Pillinger C. T. 1997. Carbon in howardite, eucrite and diogenite basaltic achondrites. *Meteoritics & Planetary Science* 32:863–868.
- Greenwood R. C., Burbine T. H., Miller M. F., and Franchi I. A. 2017. Melting and differentiation of early-formed asteroids: The perspective from high precision oxygen isotope studies. *Chemie Der Erde-Geochemistry* 77: 1–43.
- Hamilton V. E. 2000. Thermal infrared emission spectroscopy of the pyroxene mineral series. *Journal of Geochemical Research-Planets* 105:9701–9716.
- Herrin J. S., Zolensky M. E., Cartwright J. A., Mittlefehldt D. W., and Ross D. K. 2011. Carbonaceous chondrite-rich howardites: The potential for hydrous lithologies on the HED parent (abstract #2806). 42nd Lunar and Planetary Science Conference. CD-ROM.
- Jaumann R., Williams D. A., Buczkowski D. L., Yingst R. A., Preusker F., Hiesinger H., Schmedemann N., Kneissl T., Vincent J. B., Blewett D. T., and Buratti B. J. 2012. Vesta's shape and morphology. *Science* 336:687–690.
- Kebukawa Y., Nakashima S., Otsuka T., Nakamura-Messenger K., and Zolensky M. E. 2009. Rapid contamination during storage of carbonaceous chondrites prepared for micro FT-IR measurements. *Meteoritics & Planetary Science* 44:545–557.
- McCord T. B., Li J. Y., Combe J. P., McSween H. Y., Jaumann R., Reddy V., Tosi F., Williams D. A., Blewett D. T., Turrini D., and Palomba E. 2012. Dark material on Vesta from the infall of carbonaceous volatile-rich material. *Nature* 491:83.
- Miller M. F. 2002. Isotopic fractionation and the quantification of ^{17}O anomalies in the oxygen three-isotope system: An appraisal and geochemical significance. *Geochimica et Cosmochimica Acta* 66:1881–1889.
- Miller M. F., Franchi I. A., Sexton A. S., and Pillinger C. T. 1999. High precision $\delta^{17}\text{O}$ isotope measurements of oxygen from silicates and other oxides: Methods and applications. *Rapid Communications in Mass Spectrometry* 13:1211–1217.
- Mittlefehldt D. W., McCoy T. J., Goodrich C. A., and Kracher A. 1998. Non-chondritic meteorites from asteroidal bodies. In *Planetary materials*, edited by Papike J. J. Reviews in Mineralogy, vol. 36. Washington, D.C.: Mineralogical Society of America. pp. 4–195.
- Nazarov M. A., Brandstaetter F., and Kurat G. 1995. A new type of carbonaceous chondrite matter from the Erevan howardite (abstract #1031). 26th Lunar and Planetary Science Conference. CD-ROM.
- Pasteris J. 1989. In situ analysis in geological thin-sections by laser Raman microprobe spectroscopy: A cautionary note. *Applied Spectroscopy* 43:567–570.
- Perron C. and Zanda B. 2005. Meteorites: Samples of NEOs in the laboratory. *Comptes Rendus Physique* 6:345–360.
- Quirico E., Raynal P.-I., and Buorot-Denise M. 2003. Metamorphic grade of organic matter in six unequilibrated ordinary chondrites. *Meteoritics & Planetary Science* 38:795–811.
- Quirico E., Orthous-Daunay F. R., Beck P., Bonal L., Brunetto R., Dartois E., Pino T., Montagnac G., Rouzaud J. N., Engrand C., and Duprat J. 2014. Origin of insoluble organic matter in type 1 and 2 chondrites: New clues, new questions. *Geochimica et Cosmochimica Acta* 136:80–99.
- Reddy V., Nathues A., Le Corre L., Sierks H., Li J. Y., Gaskell R., McCoy T., Beck A. W., Schröder S. E., Pieters C. M., and Becker K. J. 2012. Color and albedo heterogeneity of Vesta from Dawn. *Science* 336:700–704.
- Smith M. R. 1982. A chemical and petrologic study of igneous lithic clasts from the Kapoeta howardite. Ph.D. thesis, Oregon State University, Corvallis, Oregon, USA.
- Starkey N. A., Jackson C. R. M., Greenwood R. C., Parman S., Franchi I. A., Jackson M., Fitton J. G., Stuart F. M., Kurz M., and Larsen L. M. 2016. Triple oxygen isotopic composition of the high $^3\text{He}/^4\text{He}$ mantle. *Geochimica et Cosmochimica Acta* 176:227–238.
- Suzuki A., Yamanoi Y., Nakamura T., and Nakashima S. 2010. Micro-spectroscopic characterization of organic and hydrous components in weathered Antarctic micrometeorites. *Earth, Planets and Space* 62:33–46.
- Swart P. K., Grady M. M., and Pillinger C. T. 1983. A method for the identification and elimination of contamination during carbon isotopic analyses of extraterrestrial samples. *Meteoritics & Planetary Science* 18:137–154.
- Unsalan O., Jenniskens P., Yin Q.-Z., Kaygisiz E., Albers J., Clark D. L., Granvik M., Demirkol I., Erdogan I. Y., Bengu A. S., Özel M. E., Terzioglu Z., Gi N., Brown P., Yalcinkaya E., Temel T., Prabhu D. K., Robertson D. K., Boslough M., Ostrowski D. R., Kimberley J., Er S., Rowland D. J., Bryson K. L., Altunayar C., Rangelov B., Karamanov A., Tatchev D., Kocahan O., Oshtrakh M., Maksimova A. A., Karabanalov M. S., Verosub K. L., Levin E., Uysal I., Hoffmann V., Hiroi T., Reddy V., Ildiz G. O., Bolukbasi O., Zolensky M. E., Hochleitner R., Kaliwoda M., Öngen S., Fausto R., Nogueira B. A., Chukin A. V., Karashanova D., Semionkin V. A., Yesiltas M., Glotch T. D., Yilmaz A., Friedrich J. M., Sanborn M. E., Huyskens M., Ziegler K., Williams C. D.,

- Schönbächler M., Bauer K., Meier M., Maden C., Busemann H., Welten K. C., Caffee M. W., Laubenstein M., Zhou Q., Li Q., Li X., Liu Y., Tang G., Sears D., McLain H. L., Dworkin J. P., Elsilá J., Glavin D. P., Schmitt-Kopplin P., Ruf A., Le Corre L., and Schmedemann N.; The Sariçiçek Meteorite Consortium. 2019. The Sariçiçek howardite fall in Turkey: Source crater of HED meteorites on Vesta and impact risk of Vestoids. *Meteoritics & Planetary Science*. <https://doi.org/10.1111/maps.13258>.
- Verchovsky A. B. 2017. Origin of isotopically light nitrogen in meteorites. *Geochemistry International* 55:969–983.
- Wang M. S., Paul R. L., and Lipschutz M. E. 1990. Volatile/mobile trace elements in Bholghati howardite. *Geochimica et Cosmochimica Acta* 54:2177–2181.
- Wopenka B. 1988. Raman observations of individual interplanetary dust particles. *Earth and Planetary Science Letters* 88:221–231.
- Zolensky M. E., Weisberg M. K., Buchanan P. C., and Mittlefehldt D. W. 1996. Mineralogy of carbonaceous chondrite clasts in HED achondrites and the Moon. *Meteoritics* 31:518–537.
-